
Flow, Turbulence and Combustion **69:** 3–33, 2002.

Confined and Agitated Swirling Flows with Applications in Chemical Engineering

JOS DERKSEN
Kramers Laboratorium voor Fysische Technologie, Delft University of Technology, Prins Bernhardlaan 6, 2628 BW Delft, The Netherlands

Received 25 January 2002; accepted in revised form 18 August 2002

Abstract. Turbulent, swirling flows are encountered frequently in chemical engineering practice. In this article, experiments and simulations on two classes of swirling flows, viz. agitated flows (stirred tanks), and confined swirling flows are discussed. Results of large-eddy simulations of stirred tank flow are compared with experimental data, mainly phase-resolved LDA data of the flow in the vicinity of the impeller. Next to the average velocity field, also the turbulent kinetic energy, and the anisotropy of the Reynolds stress tensor have been assessed. An important application of confined swirling flow is the cyclone separator (hydrocyclones for the separation of liquids, gas cyclones for gas-solid separation). The flow in a swirl tube geometry exhibiting many of the typical features of swirl flows (e.g. vortex breakdown) is discussed. Furthermore, a large-eddy simulation of the gas flow in a high-efficiency Stairmand cyclone separator is presented. Two examples of process modeling based on flow simulations are briefly treated: orthokinetic agglomeration of crystals in a stirred tank, and particle separation in a cyclone.

Key words: cyclone separator, large-eddy simulation, LDA, stirred vessel, swirling flow.

1. Introduction

Mixing by agitation, and separation in cyclones are two examples of the application of swirling flows in chemical engineering. In mixing, swirl is an often-unwanted side effect induced by the revolving motion of an impeller. In cyclone separators, the centrifugal force induced by swirl is the working principle. In industrial practice, the scale of the equipment, and the throughputs are such that turbulence is a key issue. It is obvious that characterization and predictive modeling of the above-mentioned flows are beneficial for economic and environmental reasons It should be noted, however, that only describing and/or modeling the flow is hardly ever sufficient for achieving process design or improvement. Phenomena like heat and mass transfer, chemical reactions, particle transport etc. need to be incorporated. Very often, their coupling with the fluid flow is of a non-linear nature, raising issues with respect to the use of Reynolds-averaged or filtered flow quantities for modeling the various processes; in principle the non-linearities in process modeling require time-dependent, and local flow information. Furthermore, quantitatively predictive process modeling requires quantitatively correct

flow field predictions: If the flow field is inaccurately predicted, there is no solid basis for further process modeling anymore. The latter issue requires accurate, and highly resolved experimental data, to serve as a means to assess the quality of the flow simulations.

In this article, I would like to introduce some of our efforts to generate flow field predictions, and gather experimental data on the two flow types mentioned above (viz. agitated flows, and confined swirling flows), with the considerations regarding the applicability in process modeling in mind, i.e. with an emphasis on confronting simulation and experiment, and on appropriately handling the coupling with other, physico-chemical phenomena. Furthermore, some examples of process modeling will be discussed.

The common features of the simulations described in this article (large-eddy simulations (LES), based on lattice-Boltzmann discretization of the Navier–Stokes equations) will be briefly explained in the next section. In Section 3, agitated flows will be treated. A three-dimensional LDA experiment will be described that measures the full Reynolds stress tensor in the turbulent wake of an impeller blade. This experiment was carried out to quantify anisotropy. Furthermore, results of LES of agitated flows will be presented. As an example of process modeling, orthokinetic agglomeration of solid particles in a turbulently agitated supersaturated liquid, relevant for industrial crystallization processes will be briefly discussed. The subject of Section 4 is confined swirling flow. Here, the experimental data is mainly from the literature [11, 12]. Simulations of flows in various confinements will be discussed. The application that will be treated is solid particle transport in a reverse-flow cyclone, a device for separating solid particles from a gas stream. The article is summarized in Section 5.

Part of the work presented here has been published, mainly in the chemical engineering literature [4–8, 18]; part is original (e.g. the assessment of stirred tank large-eddy simulations in terms of the extent of anisotropy; the flow field and particle separation results in a Stairmand high-efficiency cyclone). In case results have been published elsewhere, this is indicated by references in the text, or in the figure captions.

2. Numerical Method and Subgrid-Scale Modeling

The numerical simulations presented here are based on lattice-Boltzmann discretiation of the Navier–Stokes equations. The reason for this choice is related to some typical features of the flows we are interested in. In the first place, they generally exhibit some sort of coherent time-dependency. In the case of a stirred tank, this time-dependence is imposed by the boundary conditions: an impeller revolving inside a baffled tank; in swirling flows instabilities occur that give rise to coherent fluctuations (vortex core precession). In general, there is no clear spectral gap between the coherent, and the turbulent fluctuations. In the second place we need as detailed as possible flow information to be able to do realistic process

modeling. These considerations were the reason to attempt large-eddy simulations. LES requires fine grids, whereas the geometrical complexity of our flows requires a numerical technique that has sufficient geometrical flexibility. Lattice-Boltzmann methods largely serve these needs.

In a lattice-Boltzmann scheme, a simplified kinetic model for a Newtonian fluid is constructed that consists of a set of particles residing at the vertices of a uniform, cubic lattice, and having a discrete velocity distribution. During a single time step, the particles move from lattice site to lattice site and collide. It can be demonstrated that with suitable collision rules and lattice symmetry, the macroscopic behavior of the system resembles that of a real, Newtonian fluid, i.e. the system realizes solutions of the Navier–Stokes equation [3]. The specific scheme that was used in the present work is due to Somers [29]. It has second order accuracy in space and time. The locality of the numerical operations involved makes the scheme well suited for parallelism, which in turn allows for fine computational meshes. The shape of the flow domain does not hamper the efficiency of the method. A major disadvantage of the method (at least in the form that we apply) is the uniformity of the cubic grid, i.e. the absence of local grid-refinement.

The subgrid-scale model that has been used is the Smagorinsky model [27], with $c_s = 0.1$. Its implementation in the lattice-Boltzmann method is straightforward: instead of the molecular viscosity, the sum of the eddy viscosity and the molecular viscosity are applied during the collision step. Since the stress tensor (and therefore the deformation rate) is an intrinsic part of the lattice-Boltzmann solution vector, the locality of the operations is conserved when the subgrid-scale model is applied: there is no need to determine velocity gradients by means of e.g. finite differences.

3. Agitated Flows

The flow in a stirred tank is driven by a revolving impeller. In the process industries, stirred tanks are employed for a large variety of tasks. Examples are facilitation of chemical reactions in liquids, blending of miscible liquids, liquid-liquid dispersion of immiscible liquids, solids suspension, and gas dispersion. As a consequence, there is an enormous variety of impellers and tank layouts. Fluid dynamics research on stirred tanks has adopted a few *de facto* standard impeller and tank geometries, two of which are schematically depicted in Figure 1. In these standards, the tank is circular cylindrical, with a diameter equal to the liquid height. At the perimeter of the tank, four, 90°-spaced so-called baffles are placed to prevent solid body rotation of the flow (which would deteriorate the mixing performance, in that sense swirl is unwanted in these flows). The standard impellers have flat blades. Here, two impellers will be considered. Six vertically* oriented blades mounted on a disk constitute a so-called Rushton turbine [23], that pumps fluid in the radial direction (Figure 1a). The second impeller geometry consists of four, 45°-pitched blades, mounted on the shaft (Figure 1b). This impeller pumps axially, and in general

* In most cases, the vertical direction coincides with the axis of rotation.

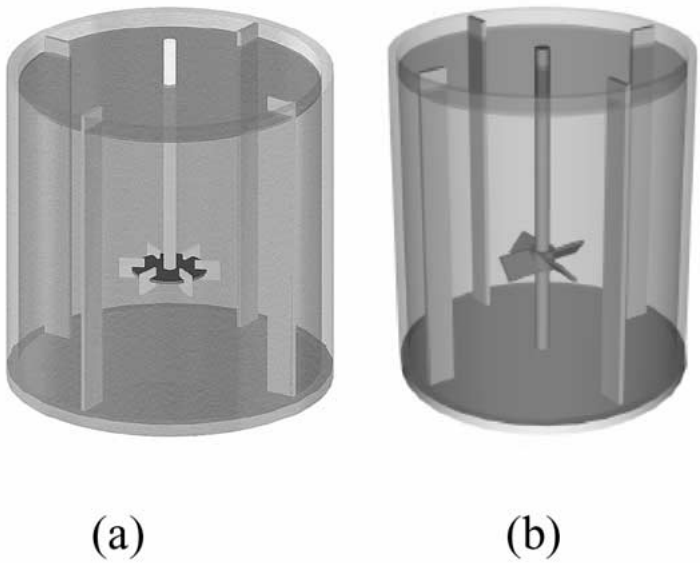

Figure 1. Standard agitated flow configurations. (a) Baffled tank with a disk turbine with six flat blades (Rushton turbine). (b) Baffled tank with a pitched blade turbine (four flat blades under a 45° angle).

rotates in such a direction that it pumps downwards. The Reynolds number for these flows is traditionally defined as $\mathrm{Re} = ND^2/\nu$, with N the rotational speed of the impeller (in rev/s), D the impeller diameter, and ν the kinematic viscosity of the liquid.

3.1. EXPERIMENTAL

Since the mid-eighties, many experimental studies in stirred tanks employing LDA have appeared in the literature [e.g. 19, 24, 34, 38, 39], more recently PIV experiments are being reported [26]. In this paper, we focus on the flow in the vicinity of the impeller, with experimental data that are impeller phase resolved (i.e. conditionally averaged with respect to the impeller orientations). One of the first papers presenting phase-resolved LDA data was by Yianneskis et al. [39]. It quantified the pair of trailing vortices in the wake of a Rushton-impeller blade, for the first time visualized by Van 't Riet and Smith [36]. In more recent papers, apart from phase-resolved average flow fields, also turbulence intensities have been measured [19].

We contributed in this field of research by performing three-dimensional LDA experiments in the wake of a Rushton turbine blade at $\mathrm{Re} = 29{,}000$; results were presented in [5]. The reason for measuring the three velocity components simultaneously was to try to assess the anisotropy of the Reynolds stress tensor. From

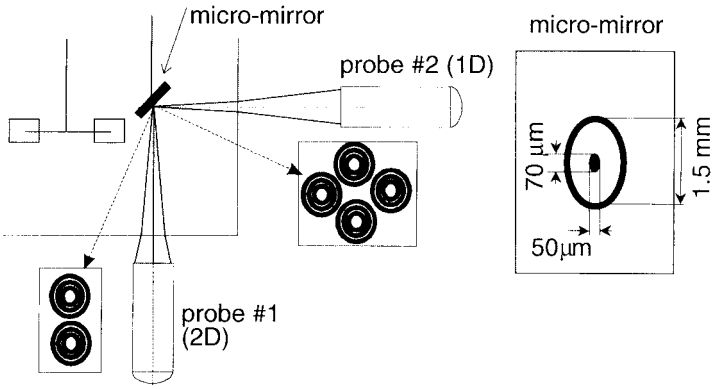

Figure 2. Experimental setup for three-dimensional LDA. Left: two fiber optic LDA probes were aligned with help of a micro-mirror. Right: dimensions of the micro-mirror. The outer elliptical ring-mirror was used to simplify finding the small mirror.

the viewpoint of flow modeling, experimental anisotropy data are a means to critically assess turbulence model performance.

The experimental setup is shown in Figure 2. The three velocity components were measured by means of two orthogonally placed optical systems (the probes in Figure 2). Probe #1 emits two beam pairs that measure the radial, and tangential velocity component; probe #2 emits one beam pair for measuring the axial velocity component. The probes also contain receiving optics. The LDA system was operated in side-scatter mode, which means that probe #1 detects the light scattered by particles traversing the measuring volume formed by probe #2, and probe #2 detects the light scattered in the (two overlapping) measuring volumes of probe #1. The key issue was to align the two probes in such a way that the three measurement volumes overlap sufficiently well to simultaneously measure the three velocity components. The fact that water was the working fluid whereas the probes were in air makes that for every measuring position in the tank the probes need to be traversed (and aligned) relative to one another. The heart of the alignment system was a micro-mirror (see Figure 2), which was submerged in the tank during alignment, and retrieved during the actual measurement. The reflective surface of the mirror was slightly smaller than the cross section of the laser beams. Once the centerlines of all six laser beams hit the center of the reflective surface, six concentric diffraction patterns are formed, indicating that alignment is achieved (Figure 3). Coincidence data-rate measurements (Figure 4) demonstrate that the maximum data rate is indeed achieved when the above alignment procedure is followed. Results of the measurements will be presented in conjunction with numerical simulations on the same flow system in the next section.

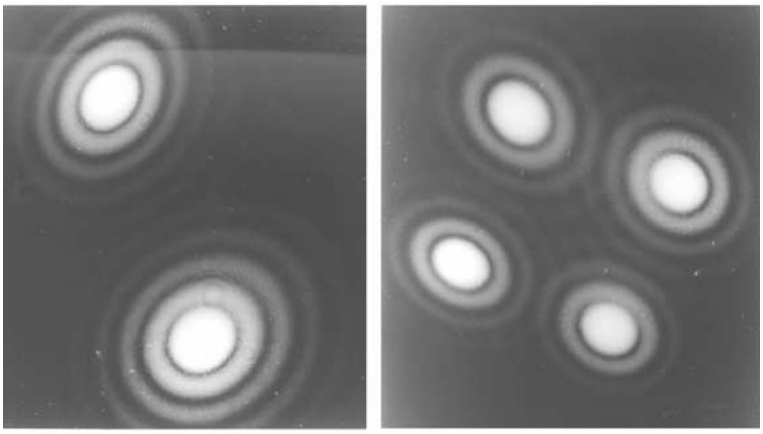

Figure 3. (a) Diffraction pattern formed by the beams emerging from probe #2 when they are both optimally reflected by the micro-mirror. (b) The same as figure (a) for the four beams emerging from probe #1.

3.2. SIMULATIONS

The impeller revolving in a static baffled tank makes stirred tank flow intrinsically unsteady. The imposed frequency (i.e. the blade passage frequency) is known to interfere with the spectrum of the turbulence induced by the impeller [38]. This, along with the demand (from the application side, see Section 1) for local, time-dependent flow information makes a large-eddy approach to turbulence modeling a favorable one. Large-eddy simulations (LES) applied to stirred tanks were first reported by Eggels [10].

In this section of the paper, a detailed comparison between our LES results, and the three-dimensional LDA experiment described in Section 3.1 is presented, with a focus on the flow in the vicinity of the (Rushton) impeller blades. The no-slip condition at the impeller surface, and at the tank wall was imposed by locally forcing the flow. This forcing technique is based on interpolation, and allows for smooth (i.e. non-staircase) walls inside the cubic grid. Details of this method can be found in [4].

In Figure 5, an impression of the overall flow in the tank is given. The average field shows that the impeller pumps the liquid in the radial direction. At the tank wall, fluid is either directed upwards, or downwards. This results in two large recirculation loops in the radial-axial plane. The slightly upwardly inclined impeller outstream is due to the axially asymmetric placement of the impeller in the tank: On average, the flow entering the impeller swept volume from below has slightly more momentum than the flow from above as a result of its shorter path through the vessel since its previous impeller passage. This momentum difference

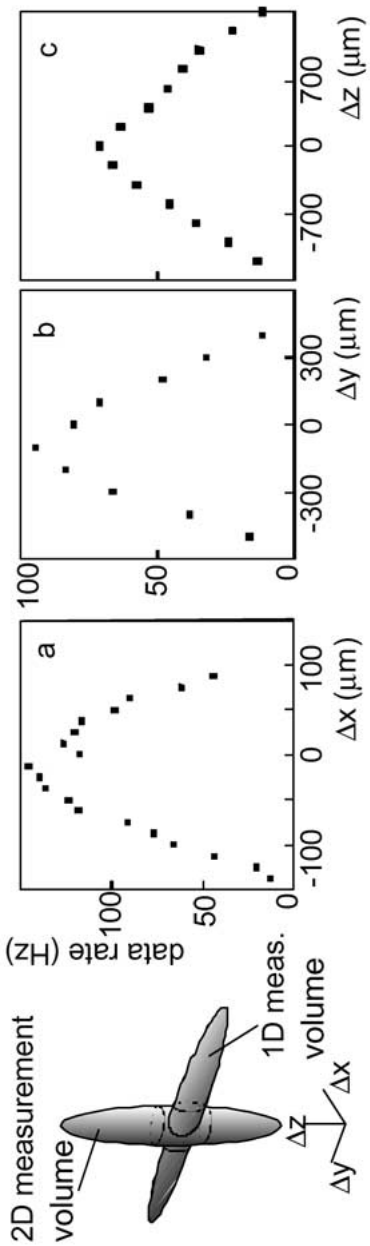

Figure 4. The data rate in coincidence mode as a function of the position of the two-dimensional measurement volume. The two-dimensional measurement volume was traversed in the three directions defined in the left rendering. The origin of all three profiles was the position of optimal alignment ($\Delta x = \Delta y = \Delta z = 0$) as found with the micro-mirror system.

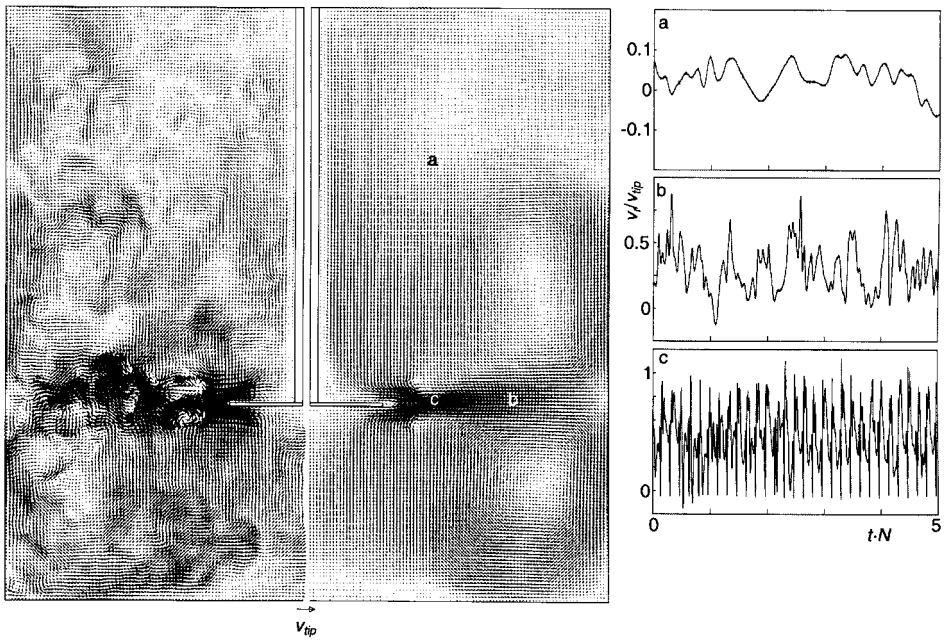

Figure 5. Left: a single realization of the flow driven by the Rushton turbine (see Figure 1a) in a vertical plane midway between two baffles in terms of velocity vectors. Center: the average flow field (averaging time: 24 impeller revolutions) in the same plane. Right: three velocity time series at different positions in the tank (as indicated in the center figure). LES on a 180^3 grid, Re = 29,000 [4].

pushes the impeller outstream slightly upwards. The turbulent, and inhomogeneous nature of the flow can be judged from the snapshot in Figure 5. Large coherent, vortical structures are formed in the wake of the impeller blades. The time series show the interplay between coherent (due to regular blade passage), and incoherent fluctuations, and the strong difference between the fluctuation levels encountered in the impeller stream, and in the bulk of the tank.

The formation of trailing vortices in the wake of the impeller blades becomes apparent if the phase-resolved average flow is considered (Figure 6). In this figure, the experimental data obtained with the three-dimensional LDA setup described in the previous section are compared with LES on two different grids. The way the clockwise rotating vortex formed behind the lower part of the blade moves radially with increasing impeller angle is well reproduced by the simulations. Note that the spatial resolution of the LES has significant impact on the quality of the predictions. The highest velocity fluctuation levels (in terms of the turbulent kinetic energy $k = (1/2)\overline{u_i u_i}$) are encountered in the region in between the lower and upper (not shown) trailing vortex (see Figure 7). In the course of the simulation it could be observed that these fluctuations are mainly due to position fluctuations of the cores of the vortices formed behind the impeller.

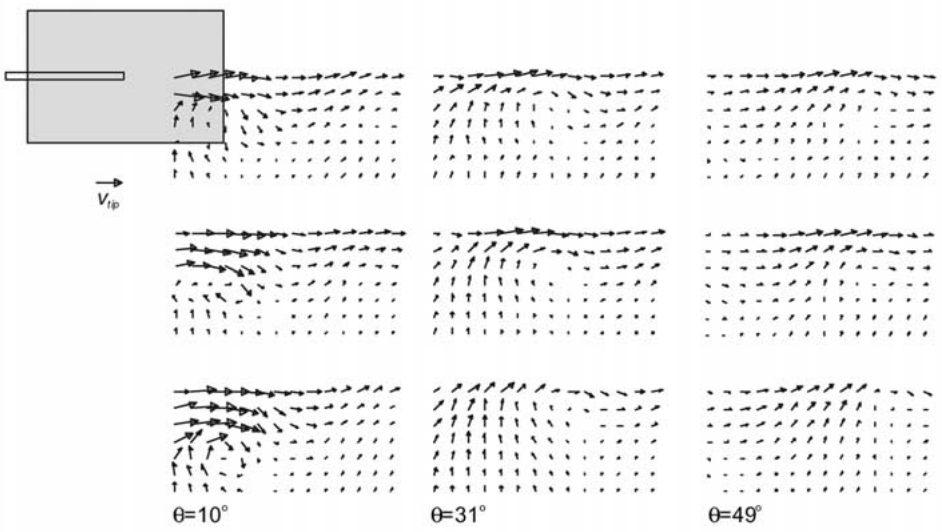

Figure 6. Phase-resolved average velocity fields at three different angles with respect to an impeller blade in the vicinity of the Rushton turbine, in the vertical plane, midway between two baffles. Re = 29,000. Comparison between experiments and LES. Top row: LDA experiments [5], middle row: LES on a 360^3 mesh, bottom row: LES on a 180^3 mesh [4]. In the top left graph, the $\theta = 0°$ position and size of the impeller blade is indicated. The LES results have been linearly interpolated to the experimental grid. The reference vector serves all vector fields.

Similar observations can be made for the flow driven by a 45°-pitched blade turbine. Here we make use of experimental data obtained by Schäfer et al. [24]. Now a single tip vortex is formed (Figure 8), that moves in axial direction. The kinetic energy levels in the vicinity of this impeller are much lower than those generated by the Rushton turbine (compare Figures 7 and 9). Relatively, the accuracy of the LES predictions regarding the kinetic energy of the flow due to the pitched blade turbine is less than that of the flow induced by the Rushton turbine. The absolute errors are comparable.

In the three-dimensional experiments, the full Reynolds stress tensor has been measured. To characterize its anisotropy, we have followed a method by Lumley [21]. First, from the Reynolds stress tensor $\overline{u_i u_j}$ the anisotropy tensor a_{ij} is derived:

$$a_{ij} = \frac{\overline{u_i u_j}}{k} - \frac{2}{3}\delta_{ij}, \tag{1}$$

with δ_{ij} the Kronecker delta function. The first invariant (i.e. the trace) of a_{ij} is (by definition) equal to zero. The second and third invariant (A_2 and A_3) read

$$A_2 = a_{ij}a_{ji}; \quad A_3 = a_{ij}a_{jk}a_{ki}. \tag{2}$$

In the two-dimensional space spanned by A_2 and A_3, a triangular shaped region (the Lumley triangle) encloses all possible states of the Reynolds stress tensor (see

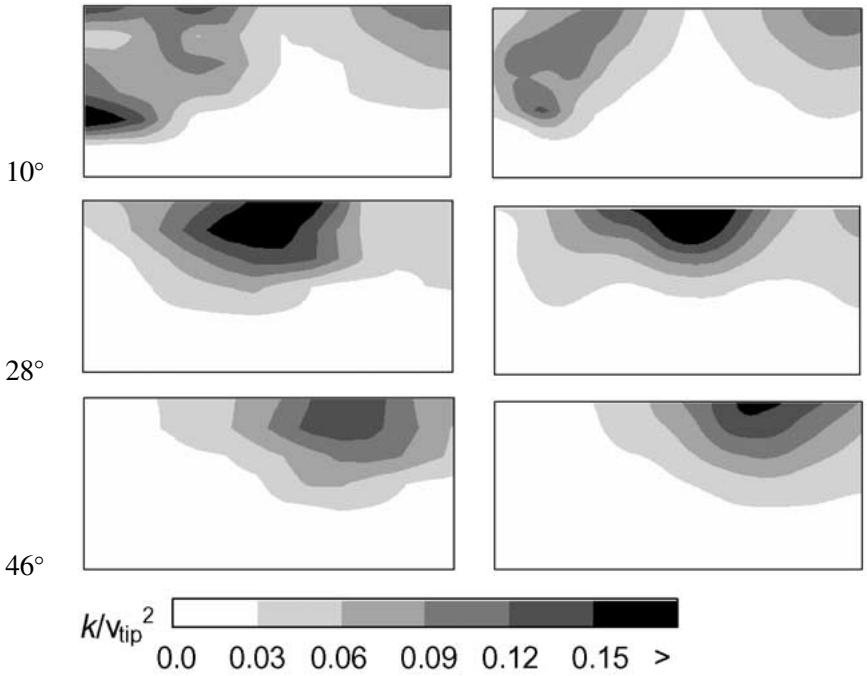

Figure 7. Phase-resolved kinetic energy fields at three different angles with respect to an impeller blade in the vicinity of the Rushton turbine (the field of view is the same as in Figure 6), in the vertical plane, midway between two baffles. Re = 29,000. Left: LDA experiments [5]; right: LES on a 180^3 grid [4].

Figure 10, top). This two-dimensional representation of anisotropy can be reduced to a one-dimensional one if it is realized that most of the anisotropy in the wake of the impeller blades is confined to a region close to the axisymmetric branch of the Lumley triangle, see [5]. As the single parameter to characterize anisotropy we have chosen the distance to the origin in the A_3–A_2 space: $|A| = \sqrt{A_2^2 + A_3^2}$. For purely axisymmetric turbulence with the kinetic energy contained in the symmetry direction being equal to the sum of the energy contained in the other two directions, $|A| = 0.17$.

In Figure 10, some of the experimental results are presented, along with LES results. The distribution of $|A|$ in the experiment is not very coherent. Close to the blade (small angels) the flow is more anisotropic than further away from the blade; the vicinity of the vortex core also has relatively high $|A|$-levels. The LES shows an even less coherent image. Furthermore it clearly overestimates the extent of anisotropy (typically by a factor of two to three). Some of the structures observed experimentally, however, can be identified in the LES results.

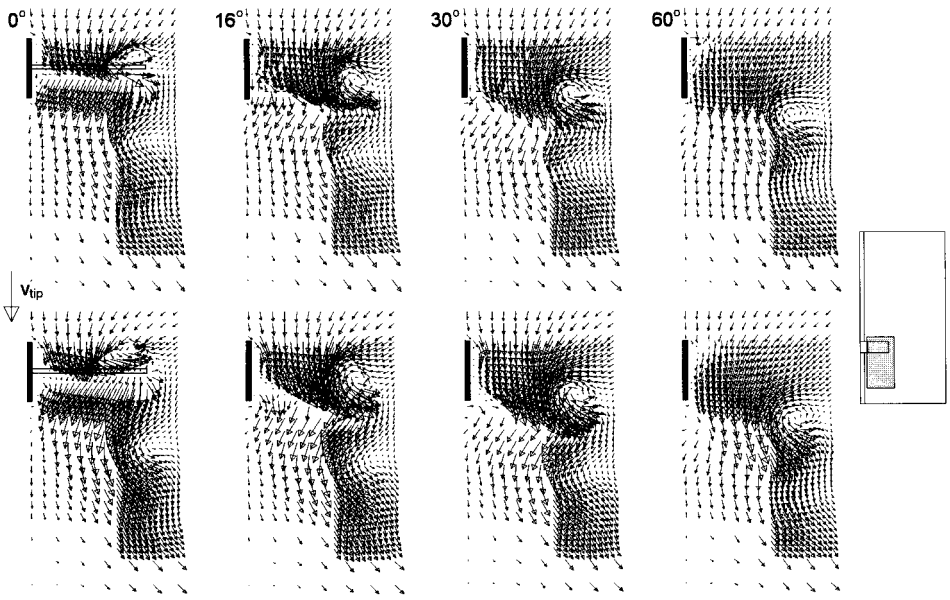

Figure 8. Phase-resolved velocity field at four different impeller angles in the vicinity of the 45°-pitched blade turbine (the field of view is indicated in the right diagram) at Re = 7,300. Top row: experiments [24]. Bottom row: LES on a 240^3 grid [7]. The reference vector serves all vector plots.

3.3. APPLICATION: ORTHOKINETIC AGGLOMERATION OF CRYSTALS

As an application of stirred tank simulations, consider the situation of orthokinetic agglomeration of particles. In industrial crystallization, crystals (e.g. salts, pigments) are formed in a supersaturated liquid that is pumped through, and agitated in vessels. Agglomeration (i.e. the merger of two crystals into a bigger one) influences the product quality. Most often, it is an unwanted phenomenon since it tends to broaden the crystal size distribution. If crystallite particles have sizes of the order of 10 μm, crystal-crystal collisions are mainly due to velocity gradients in the liquid. Agglomeration occurs when during a collision event the crystals are cemented due to the supersaturated liquid they are in. If the bond between the two crystals is strong enough, it can stand the disruptive forces (again due to velocity gradients) after the collision. This sequence of events (collision, cementing, and possibly disruption) makes the agglomeration rate J (the number of collision events per unit volume and time) strongly non-linearly dependent on the local velocity gradients:

$$J = \beta(\dot{\gamma})n^2, \tag{3}$$

with n the particle number concentration, and $\beta(\dot{\gamma})$ the agglomeration kernel as a function of the shear rate $\dot{\gamma}$ (in a first approximation, β can be considered to be independent of the particle size). The result of a theoretical model for agglomeration

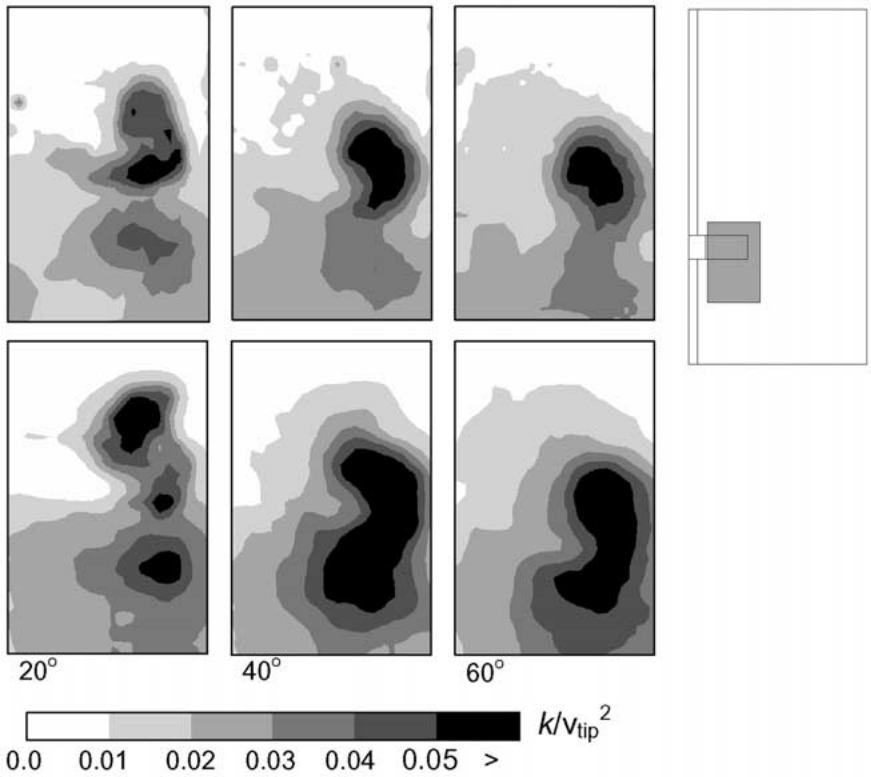

Figure 9. Phase-resolved contour plots at three different impeller angles of the turbulent kinetic energy in the vicinity of the pitched blade turbine (the field of view is indicated in the right diagram) at Re = 7,300. Top row: experiments [24]. Bottom row: LES on a 240^3 grid [7].

in simple shear flow [22] is summarized in Figure 11. At low shear rates, the agglomeration kernel is dominated by the collision frequency, which is proportional to the shear rate. Here, every collision leads to an agglomerate due to the weak disruptive forces. The higher the shear rate, the less effective the collisions get, and the more β deviates from linearity with respect to shear.

In order to model agglomeration in stirred tanks, the LES code was supplemented with a Monte-Carlo algorithm that solved the transport equation for the number density n [18]. In the transport equation, agglomeration acts as a sink. The local, time-dependent shear rate, necessary to determine the local value of β in the particle number transport equation was estimated from the LES through the deformation rate⋆:

$$\dot{\gamma}^2 \approx \frac{1}{2}\left(\frac{\partial u_i}{\partial x_j} + \frac{\partial u_j}{\partial x_i}\right)^2. \tag{4}$$

⋆ In a more refined model, the grid-scale deformation was taken into account as well [18].

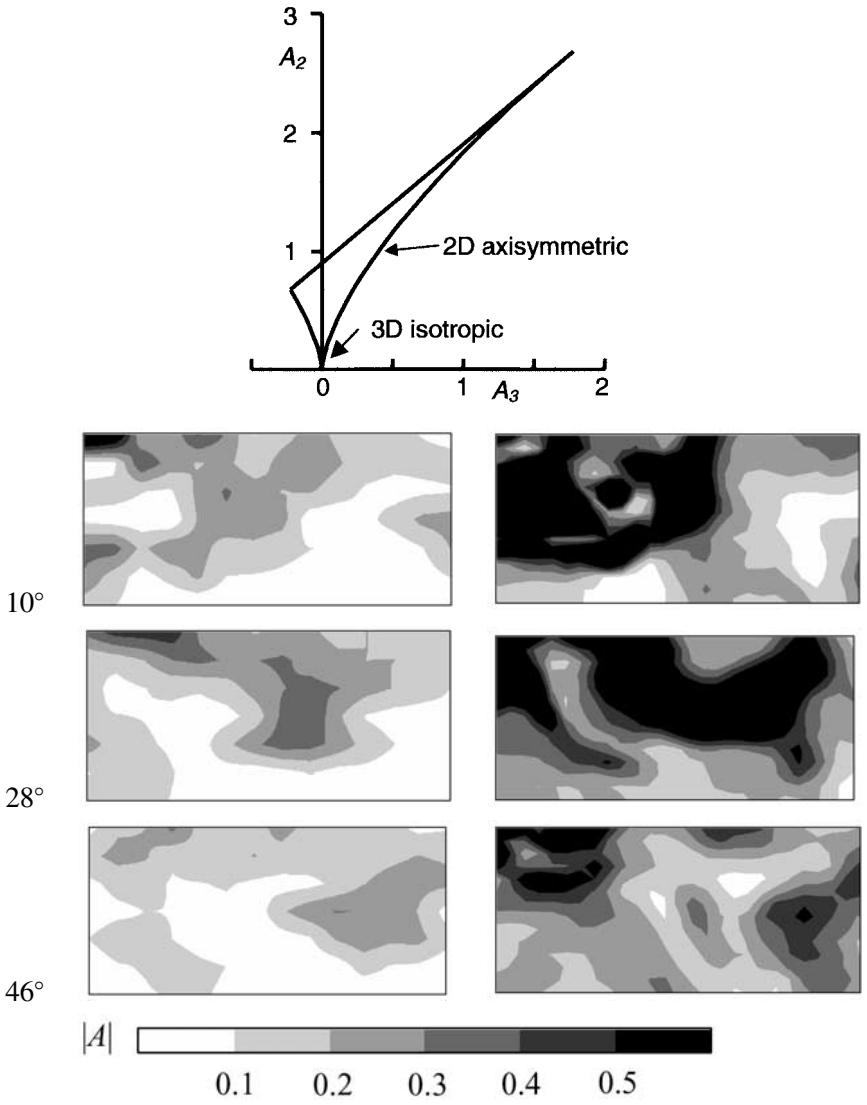

Figure 10. Top: Lumley triangle. Bottom: phase-resolved anisotropy fields (in terms of $|A| = \sqrt{A_2^2 + A_3^2}$) at three different angles with respect to an impeller blade in the vicinity of the Rushton turbine (the field of view is the same as in Figure 6), in the vertical plane, midway between two baffles. Re = 29,000. Left: experiments [5]; right: LES on a 180^3 grid.

Figure 12 shows for the specific crystal system of Figure 11 the inhomogeneous distribution of the agglomeration rate kernel throughout the tank. The time-averaged part indicates that hardly any agglomeration occurs in the volume swept by the impeller. Apparently deformation rates close to the impeller are too high to cause agglomeration. The single-realization shows how the turbulent flow structures trans-

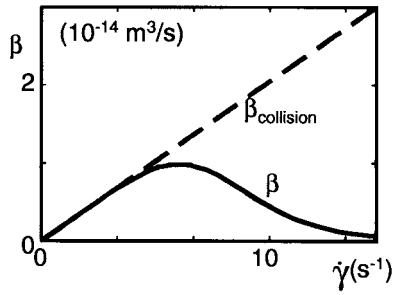

Figure 11. The agglomeration kernel β (as defined in Equation (3)) in simple shear flow as a function of the shear rate, theoretical model due to Mumtaz et al. [22] for $CaO_x \cdot H_2O$ crystals. For reference, the collision kernel $\beta_{\text{collision}}$ is indicated.

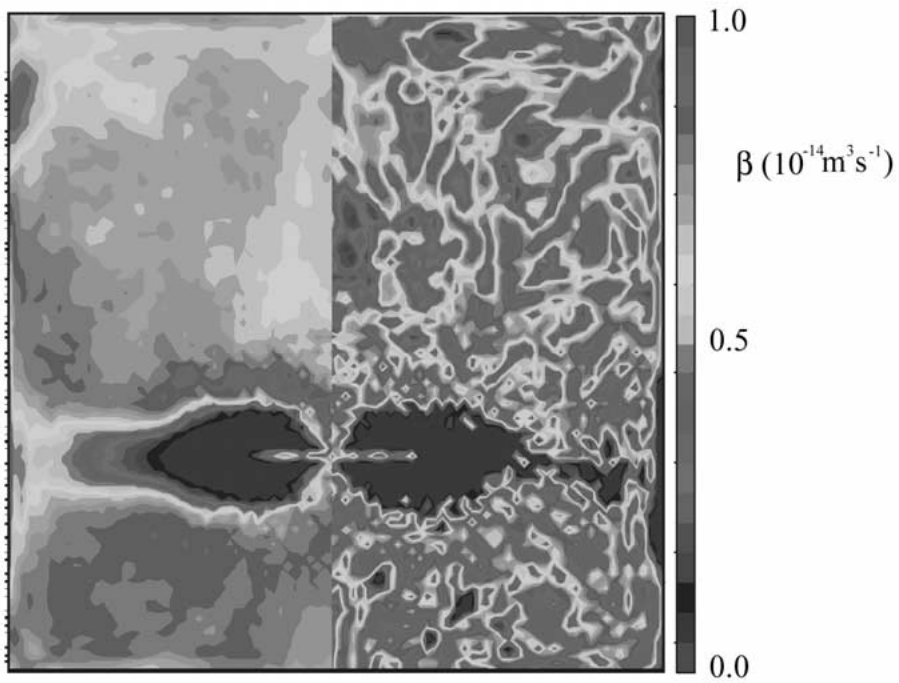

Figure 12. The distribution of the agglomeration kernel β throughout the vertical plane midway between two baffles in an agitated tank driven by a Rushton turbine. Left: time-averaged values; right: single realization [18].

late into a spatial β-distribution. The way the tank-volume average agglomeration is affected by the fluid flow is summarized in Figure 13. The symbols are various simulation results (different Reynolds numbers, and tank geometries) in which for the agglomeration kernel the drawn line was adopted (i.e. Figure 11 on a logarithmic scale). The dashed line is a "fit" through the data points, and represents in a way the classical method in chemical engineering for measuring agglomeration

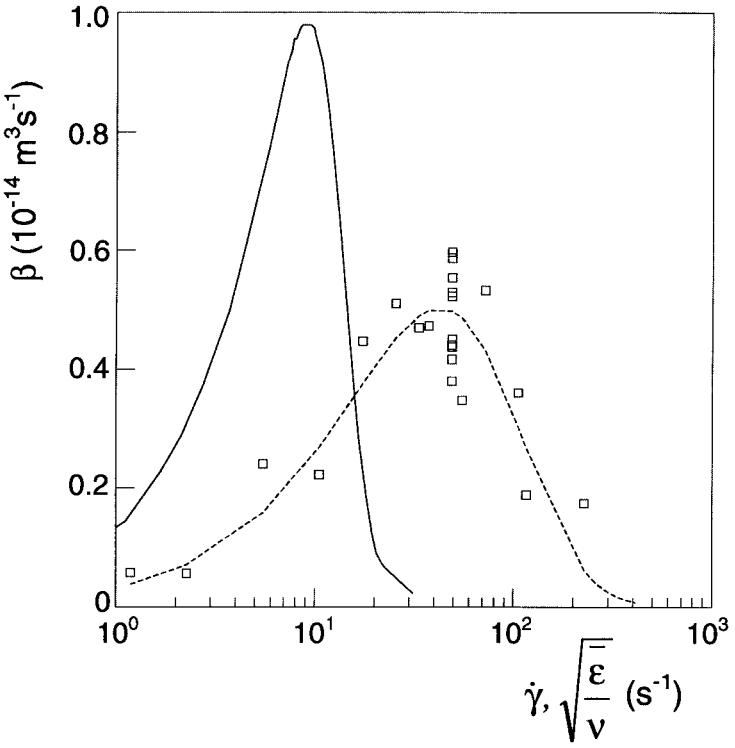

Figure 13. Solid line: same as Figure 11, with $\dot{\gamma}$ on a logarithmic scale. Symbols: tank-averaged agglomeration kernels (various tank sizes and impeller geometries) as a function of the tank-averaged deformation rate $\sqrt{\overline{\varepsilon}/\nu}$ [18]. Dashed line: fit through the symbols with the same mathematical expression as used for the solid line.

kernels: Measure the decrease in number concentration in a stirred vessel as a function of the tank-averaged deformation rate (estimated from the tank-averaged energy dissipation rate $\overline{\varepsilon}$, i.e. the power drawn by the impeller divided by the total liquid mass). The huge discrepancy between the solid and dashed curve shows that measuring agglomeration this way is strongly biased by hydrodynamic effects as a result of the non-linearities involved.

4. Confined Swirling Flows

Our interest in confined swirling flows relates primarily to gas-solid cyclone separators [16]. These are simple devices (no moving parts) to separate solid particles from gas streams. Cyclones cover a broad spectrum of applications: In the oil industry they are applied extensively in e.g. oil-water separation, or in Fluid Catalytic Cracking (FCC) units to recover catalyst particles, the scale of the latter equipment being of the order of 10 m; in domestic applications they are used as part of a vacuum cleaner [9] with sizes of the order of 10 cm.

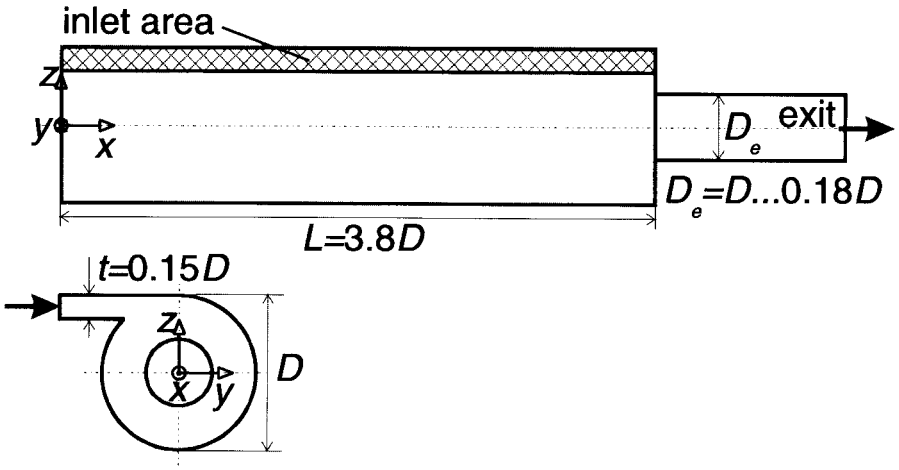

Figure 14. Swirl tube geometry as defined in [11]. Fluid enters through a tangential slit, and exits through a contraction.

In the first part of this section, a swirl-tube geometry will be discussed on which Escudier et al. [11] performed visualization and LDA experiments. The experimental data have been used to assess numerical simulations, especially with respect to grid effects. The subsequent parts treat a reverse-flow cyclone geometry, including a numerical particle separation study.

4.1. SWIRL TUBE

The specific vortex tube geometry discussed here was defined in an experimental study by Escudier et al. [11], see Figure 14. In this flow system, the Reynolds number is based on the inlet slit width t, and the superficial inlet velocity U_{in}: $\text{Re} = tU_{\text{in}}/\nu$. The common feature with cyclone separators is the generation of swirl by means of a tangential inlet channel. In contrast to the commonly generated reverse flow (inlet and outlet at the top, see Figure 19) in a gas cyclone, the vortex tube facility generates a uni-directional flow. By means of flow visualization and extensive LDA experiments, Escudier and co-workers showed the strong impact of an exit pipe contraction on the entire flow field. Furthermore, vortex breakdown was observed inside, or slightly upstream of the exit pipe. A third important observation when visualizing the flow was the clear distinction between the vortex core region where radial mixing is strongly suppressed, and the outer region that shows turbulent vortical structures (Taylor–Görtler vortices [12]).

Swirling flows exhibiting vortex breakdown have been the subject of many numerical studies. Lopez and co-workers have reported detailed axisymmetric simulations on the flow in a cylindrical container with one rotating end wall (see [20], and the references therein). The extension to three-dimensional simulations in a similar geometry has been made by Sotiropoulos and Ventikos [30, 31] and

by Serre and Bontoux [25]. These were direct simulations (i.e. without the use of turbulence modeling) in closed containers (i.e. no inflow/outflow boundaries). Reynolds numbers (based on the velocity of the perimeter of the rotating end wall, and the radius of the container) are in the range 10^3–10^4. Snyder and Spall [28], and Spall and Ashby [32] simulated swirling flows in pipes undergoing breakdown. The former article again describes a direct simulation (Re $=$ 2,000). In [32], axisymmetric RANS based modeling is applied to swirling tube flow at Reynolds numbers of the order of 10^5. The performance of the k–ε model was compared with that of a Reynolds Stress Model (RSM), showing favorable results for the latter.

The same method as used for simulating stirred tank flow was applied for numerically studying the flow in the Escudier-geometry for three values of the exit pipe diameter over swirl tube diameter ratio (viz. $D_e/D = 0.73$, 0.45, and 0.33). For subgrid-scale modeling, again the Smagorinsky model [27] with $c_s = 0.1$ was applied. In this flow system, it appeared to be essential to implement wall-damping functions to bring the eddy-viscosity to zero at the no-slip walls. Functions due to Van Driest (see e.g. [15]) have been used. In the LES, the outlet duct was terminated with a $\partial/\partial x = 0$ boundary condition for all flow variables. In most cases this outlet condition served well, which is remarkable in the light of the subcriticality [12] of the strongly swirling flow at the (numerical) outlet plane. Subcriticality allows disturbances to propagate upstream and therefore it may be expected that the results are sensitive to the outflow boundary condition. In [11] no details are given on how in the experiment the flow was terminated.

A quantitative assessment of the simulations is based on the average radial velocity profiles measured by Escudier et al. [11]. In the LDA experiments, special care was taken to traverse the measurement volume through the center of the vortex core (defined as the position in the y–z plane with zero tangential and radial velocity), which not necessarily coincided with the geometrical center of the tube. The vortex center has a spiraling shape (see Figure 15). In this figure, the time-averaged center of the vortex as a function of the axial coordinate x inside the swirl tube as determined by Escudier (six data points per geometry), and by means of the LES is shown. Experiment and simulation qualitatively agree. Note that in the LES the vortex center has a slightly wavy shape. The experimental points are too coarsely spaced to judge if this shape is related to reality. Also the vortex core visualizations in [11] are inconclusive on this issue.

In the LES the time-dependence of the vortex center position was investigated. The position of the vortex center was remarkably stable. Only fluctuations at subgrid level were detected: the RMS value of the z-coordinate of the vortex center for the case with $D_e/D = 0.45$ was $0.005D$ (this value was hardly a function of the axial location in the vortex tube), whereas the grid spacing was $0.0076D$.

The radial profiles of the swirl velocity component (Figure 16) have a shape similar to Burgers' [2] solution, which was based on the assumption of a uniform axial velocity distribution. The actual axial velocity profiles are, however, far from uniform (see Figure 17). The geometrical ratio D_e/D has strong impact

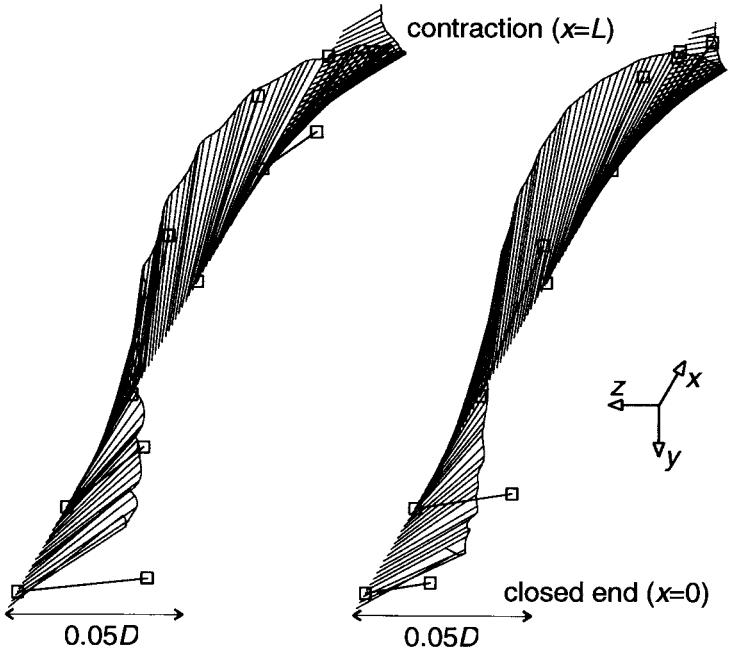

Figure 15. Time averaged position of the vortex center. Left: $D_e/D = 0.45$; right $D_e/D = 0.33$. The square symbols indicate the experimentally determined positions [11], the drawn lines are LES results [8].

on the tangential velocity levels: the maximum tangential velocity increases significantly, and the diameter of the vortex core (as a measure for the latter we take the distance between the two extremes in the profile) reduces if D_e/D is reduced. As a consequence, velocity gradients at $D_e/D = 0.33$ are much higher than at $D_e/D = 0.73$. This observation is reflected in the performance of the LES. The agreement between simulation and experiment is good for $D_e/D = 0.73$, and for $D_e/D = 0.45$. The levels of maximum tangential velocity, and the vortex core diameter correspond with the experimental data. In general, the agreement gets better for higher spatial resolution. Spatial resolution effects are most pronounced for the smallest D_e/D ratio ($D_e/D = 0.33$). In this case, the LES profiles are less pronounced than the experimental ones, leading to an underestimation of the maximum velocity levels. We might be able to improve the sharpness of the LES profiles by using a more sophisticated subgrid-scale model. It has been observed that the vortex core behaves like a laminar flow [12], in which the Smagorinsky model most likely overestimates the eddy-viscosity. By using a model that switches off at low mesh Reynolds numbers (such as the model proposed by Voke [37]) the excessive damping by the Smagorinsky model can be avoided, and higher gradients might appear in the velocity profiles.

The shape of the radial profiles of the axial velocity component (Figure 17) strongly depends on the ratio D_e/D, and on the axial position in the vortex tube.

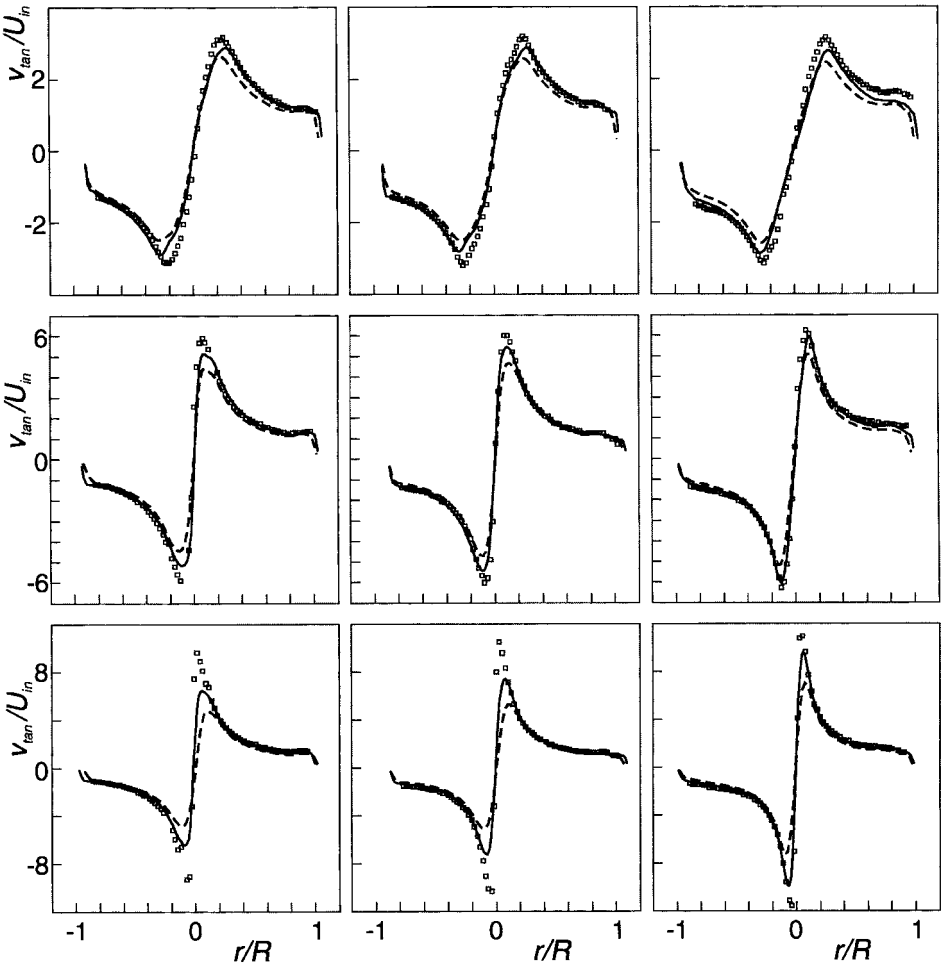

Figure 16. Tangential velocity profiles. From top to bottom: $D_e/D = 0.73$, $D_e/D = 0.45$, and $D_e/D = 0.33$. From left to right: $x/D = 0.15$, 2.15, and 3.61. The symbols denote experimental data [11]. The dashed line is the LES result with a spatial resolution such that $\Delta = D/82$, the solid line with $\Delta = D/132$ [8]. $R = D/2$.

The width of the axial velocity profiles appears to be related to the diameter of the vortex core. The pressure field is thought to be responsible for this tight coupling between the axial and tangential velocity. The radial pressure distribution induced by the swirl component, and its axial variation strongly influences the axial velocity. The profiles for $D_e/D = 0.73$, and $D_e/D = 0.45$ show an axial velocity deficit near the axis, whereas at $D_e/D = 0.33$ the profiles show a single, and sharp peak. The sensitivity of the LES with respect to the spatial resolution now becomes apparent already at $D_e/D = 0.45$. The lower resolution simulation underestimates, or even misses the velocity deficit in the very core of the flow, whereas the higher resolution is capable of representing it fairly well.

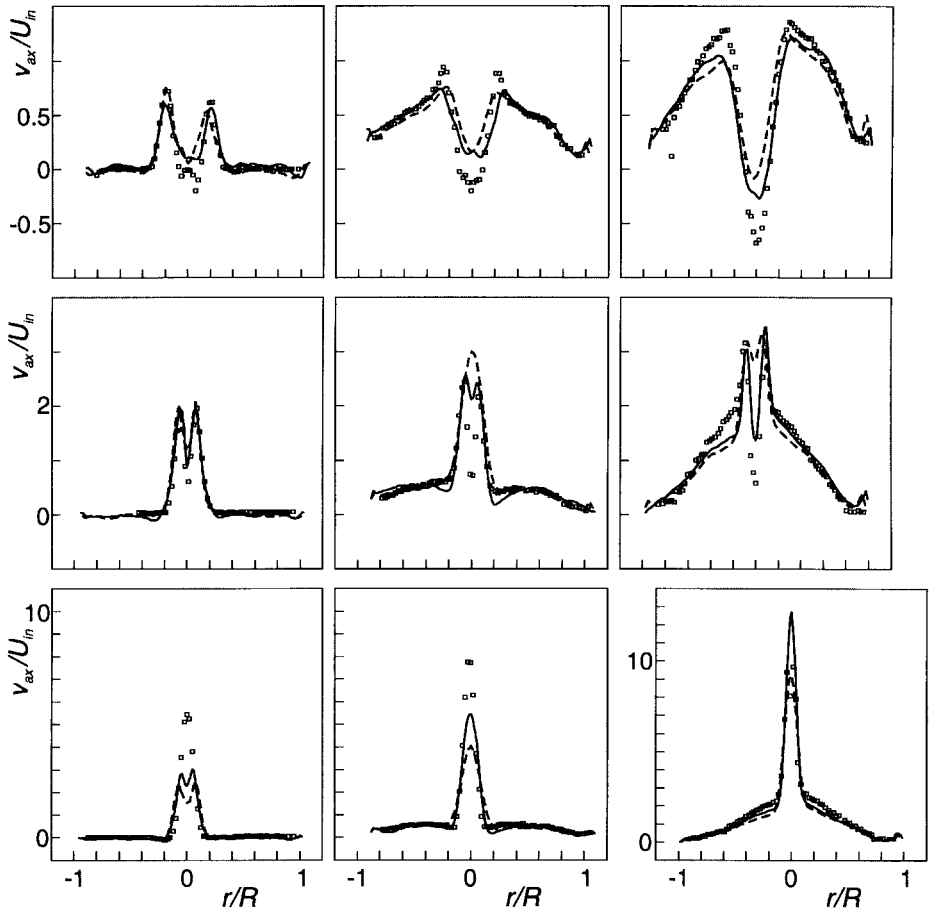

Figure 17. Axial velocity profiles. From top to bottom: $D_e/D = 0.73$, $D_e/D = 0.45$, and $D_e/D = 0.33$. From left to right: $x/D = 0.15$, 2.15, and 3.61. The symbols denote experimental data [11]. The dashed line is the LES result with a spatial resolution such that $\Delta = D/82$, the solid line with $\Delta = D/132$ [8]. $R = D/2$.

Under certain conditions, the flow exhibits vortex breakdown (see Figure 18). The occurrence and type of breakdown depends on the flow geometry (in this study the ratio D_e/D), and the flow rate [13]. The experimental visualizations in Figure 18 indicate a bubble type breakdown (Type 0 in the classification by Faler and Leibovich [13]) in both geometrical cases. For $D_e/D = 0.33$, the LES has approximately the same Reynolds number as the experiment. It clearly shows the Type 0 breakdown, with a single, thin tail. The bubble is filled and emptied simultaneously at the rear part (see the vector plot in Figure 18). For $D_e/D = 0.45$, there is less correspondence between experiment and LES. This might very well be due to the difference in Reynolds number. In [11] an upstream migration of the

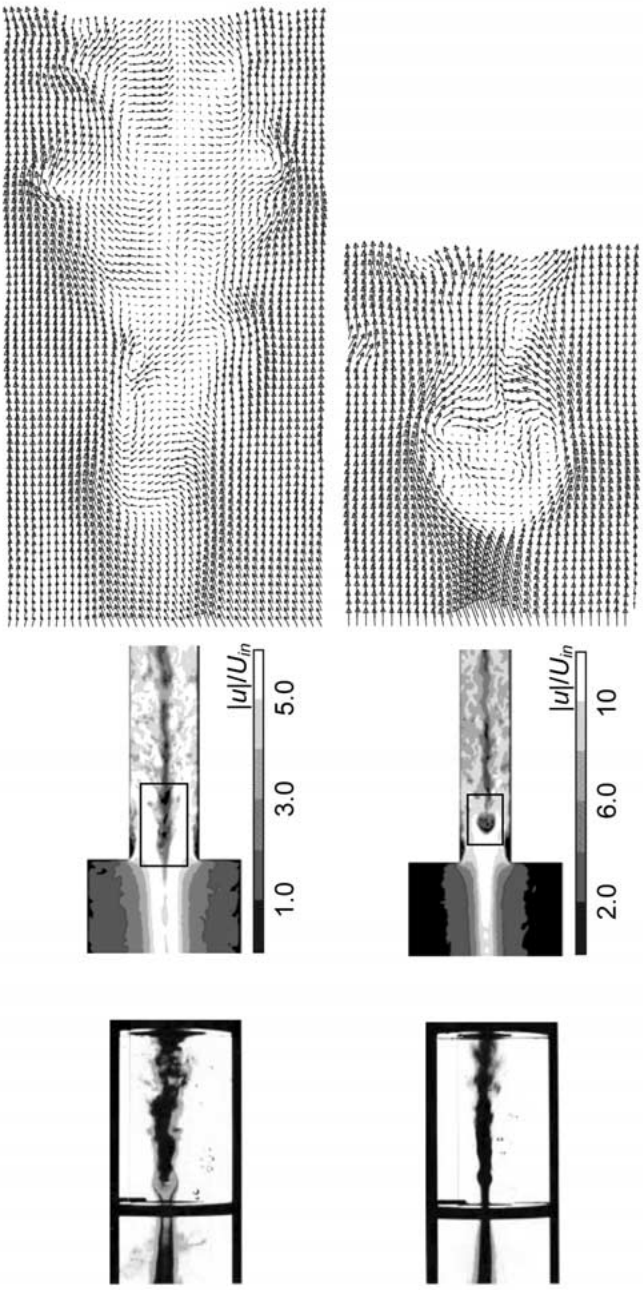

Figure 18. Vortex breakdown for $D_e/D = 0.45$ (top), and $D_e/D = 0.33$ (bottom). Left: visualization as reported in [11] at $\mathrm{Re} = 650$ (top), and $\mathrm{Re} = 1{,}600$ (bottom). Center: LES snapshot in terms of the contours of the absolute value of the velocity near the contraction at $\mathrm{Re} = 1{,}900$. Right: the velocity vector field at the position as indicated with the rectangles in the center pictures.

breakdown when increasing the Reynolds number was experimentally observed. In the LES at $D_e/D = 0.45$, the breakdown appears to be of Type 1 (compared to Type 0, Type 1 has a less regular shape and thicker tail, but still a stagnation point at the front side). Faler and Leibovich [13] indeed report Type 0 to Type 1 transitions when increasing the Reynolds number.

4.2. REVERSE FLOW CYCLONE

The Stairmand high-efficiency cyclone [33] is mainly used for fine (μm) particle separation. Its geometry is depicted in Figure 19. In our laboratory, LDA experiments have been performed on its gas flow field at $\mathrm{Re} = 280{,}000$ (with the Reynolds number defined as $\mathrm{Re} = U_{\mathrm{in}} D/\nu$) [17]. In contrast to the swirl tube geometry of Section 4.1, LES of the Stairmand geometry with the outlet boundary condition $\partial/\partial x = 0$ appeared to cause unphysical phenomena at the outlet plane that propagated upstream. This was probably caused by the subcriticality of the flow at the outlet plane [12]: the not fully physically correct outflow boundary condition has influence on the entire flow system. For now, we circumvented this problem by placing an obstruction (a round disk) in the exit pipe (see Figure 19) that caused a sub- to supercritical transition (an effect anticipated by Benjamin [1]). It was checked, and confirmed that details of the obstruction (size and position) had hardly any influence on the velocity field inside the cyclone. In future simulations it will be investigated if e.g. a convective outflow boundary condition $((\partial/\partial t) + U_c(\partial/\partial x) = 0)$ shows better behavior.

The average tangential velocity profiles as measured (and simulated) look very similar to the ones observed in the swirl tube geometry (previous section). A Burgers-type vortex [2] adequately covers the radial distribution of the swirl velocity (see Figure 20). The axial velocity profiles show the reverse-flow character of the cyclone: downward flow close to the outer wall, upward flow in the center. Also this swirling flow has an axial velocity deficit near the core of the vortex.

Measurements of the RMS values of the tangential and axial velocity components (Figure 20) point at the presence of vortex core precession: increased fluctuation levels in the vortex core, and a seemingly positive correlation of the fluctuation levels with the average velocity gradients. The issue of vortex core precession was further investigated by considering simulated velocity time series, and vortex center positions. The fluctuations induced by vortex core precession are often of a (quasi-) periodic nature (the vortex whistle, see e.g. [14]). More or less coherent velocity fluctuations were indeed observed (see Figure 21). A spectral analysis of the time series shows a distinct peak at a frequency $f = 1.7 \cdot U_{\mathrm{in}}/D$ (in other words, the Strouhal number $\mathrm{St} = fD/U_{\mathrm{in}} = 1.7$). Apparently the geometry of the flow's confinement has strong impact on the presence, frequency, amplitude, and coherence of vortex core stability: the swirl tube of the previous section showed a very stable vortex, whereas earlier cyclone simulations [6] showed (compared to the Stairmand cyclone) much stronger and more coherent oscillations at $\mathrm{St} = 0.5$.

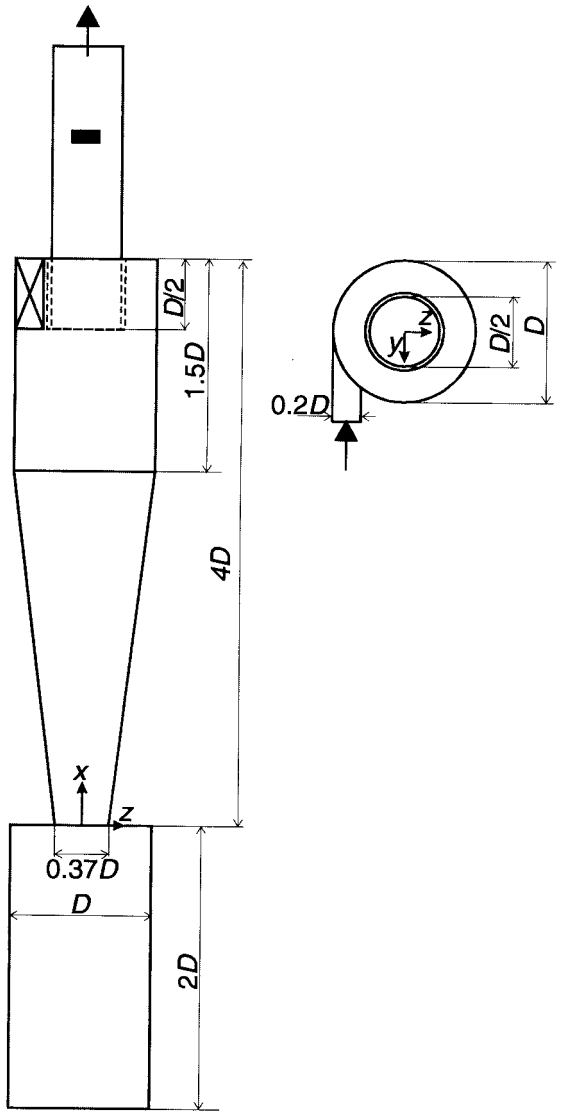

Figure 19. Stairmand high-efficiency cyclone geometry and coordinate system. The black rectangle in the exit pipe is an obstruction that was inserted in the simulations only.

The behavior of the vortex center as a function of the axial position in the cyclone is illustrated in Figures 22 and 23. On average, the vortex center spirals around the geometrical center. The largest distances from the geometrical center are in the lower part, which is the part of the cyclone where the solid particles are collected (the collection bin). Inside the collection bin the vortex is most stable: the lowest RMS values of position fluctuations are encountered here (Figure 23). Closely above the collection bin (in the narrow part of the cone), and at the entrance

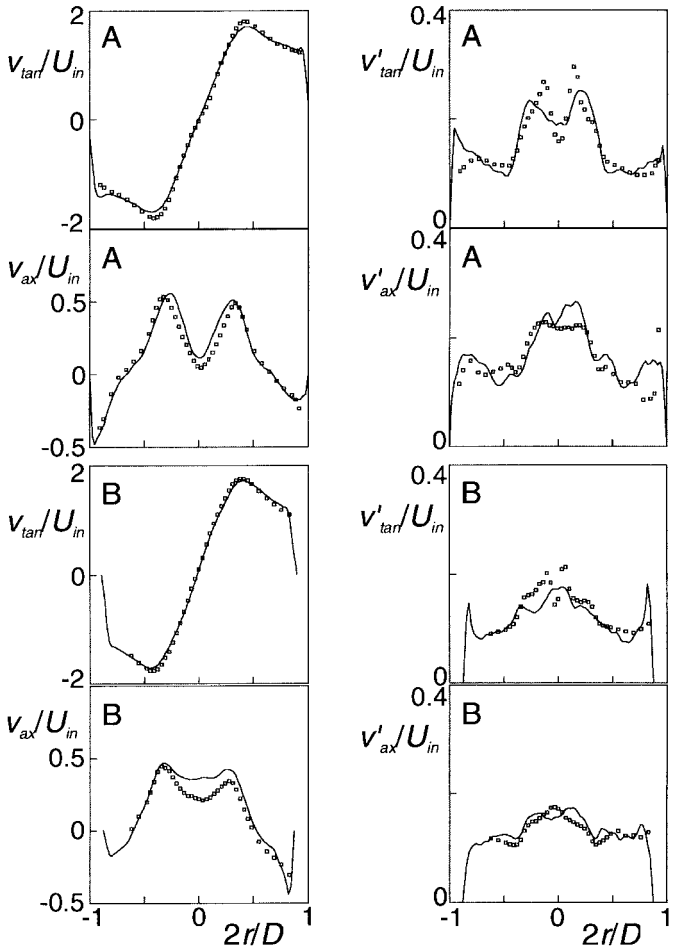

Figure 20. Radial velocity profiles in the Stairmand high-efficiency cyclone at Re = 280,000. Symbols: LDA experiments [17]; solid lines: LES. Left: average velocity; right: RMS velocities. A and B denote the axial levels. A: $x/D = 3.25$; B: $x/D = 2.0$.

of the exit pipe, the most virulent vortex core motion is observed. The discontinuities inside the exit pipe in Figures 22 and 23 are due to the presence of the obstruction to bring the flow to a supercritical state before reaching the outlet plane.

4.3. Particle collection efficiency calculations in a Stairmand high-efficiency cyclone

To numerically study the collection efficiency of the high-efficiency Stairmand cyclone, particles were released in the LES flow field. If a buoyancy force on the particles is neglected (which is a fair assumption given the large density difference between gas and solids), and if a one-way coupling between solids and gas flow

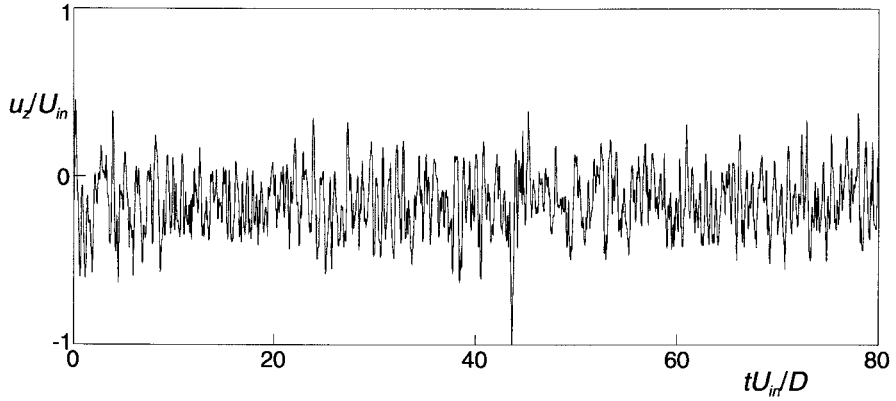

Figure 21. LES time series of the z-component of the velocity in the (geometrical) center of the Stairmand cyclone at $x/D = 2.0$.

is assumed (which is a less fair assumption since in practice mass loading ratios $\Phi_{m,\text{solids}}/\Phi_{m,\text{gas}}$ easily exceed unity, i.e. solid volume fractions typically are 10^{-3}), four dimensionless numbers determine the particle separation process: the overall flow's Reynolds number (Re, defined above), the particle's Reynolds number ($\text{Re}_p = d_p|\mathbf{v}_p - \mathbf{u}|/\nu$, with d_p the particle diameter, $\mathbf{u}$ the gas velocity and $\mathbf{v}_p$ the particle velocity), the particle's Stokes number ($\text{Stk} = (\rho_p/\rho_g)(d_p^2 U_{\text{in}}/18\nu D)$, and the Froude number ($\text{Fr} = (U_{\text{in}}^2/D|\mathbf{g}|$, with $\mathbf{g}$ the gravitational acceleration). In case the drag force on the particles obeys Stokes law (i.e. $\text{Re}_p < 1$), the gas-particle system becomes independent of Re_p.

At Re = 280,000, and Fr = 90, 23 sets each consisting of 12,000 identical, spherical particles were tracked through the cyclone. The 23 Stokes numbers⋆ are in the range $\text{Stk} = 5 \cdot 10^{-6}$ to 0.39. The particles were released at the inlet area, where they were uniformly distributed. The total time interval over which particles were fed to the cyclone extended over $18T_{\text{int}}$, with the integral time scale defined as $T_{\text{int}} = D/U_{\text{in}}$. Every time step, the particle positions were updated according to the following equation:

$$\frac{\mathrm{d}v_p}{\mathrm{d}t} = \frac{U_{\text{in}}}{\text{Stk}\ D}(\mathbf{u} - \mathbf{v}_p) + \mathbf{g}. \tag{5}$$

In the LES, the gas velocity is composed of a resolved part, and a subgrid-scale part. The former was determined by linear interpolation of the velocity field at the grid nodes to the particle position, the latter is mimicked by a uniform random process with zero average and an RMS value u_{sgs} that amounted to [35]:

$$u_{\text{sgs}} = \sqrt{\frac{2}{3}k_{\text{sgs}}}; \quad k_{\text{sgs}} = \frac{C_{\nu t}}{C_\epsilon}\Delta^2|\mathbf{S}|^2, \tag{6}$$

⋆ Here, the Stokes number mainly acts as a (dimensionless) particle size.

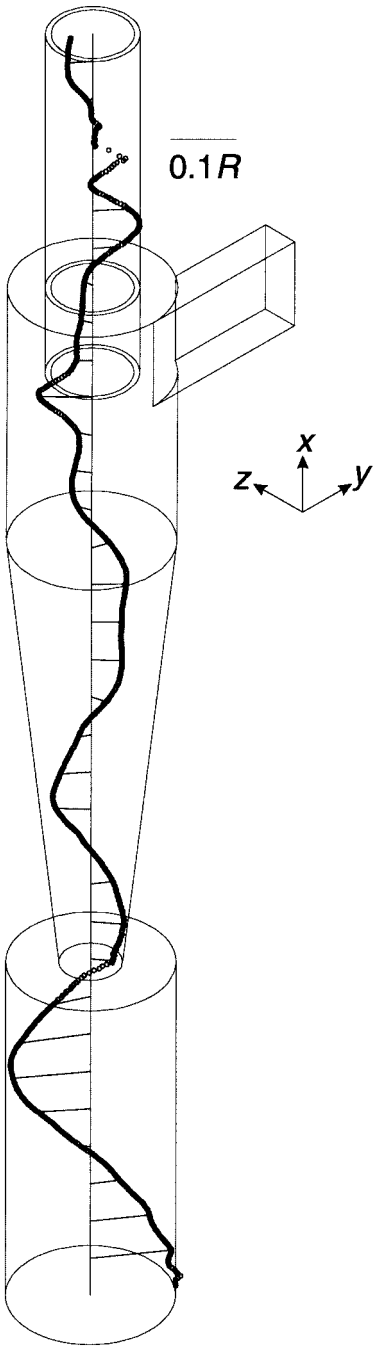

Figure 22. Isometric plot of the average position of the vortex center in the Stairmand cyclone according to the LES. Note that transverse displacement is not on scale.

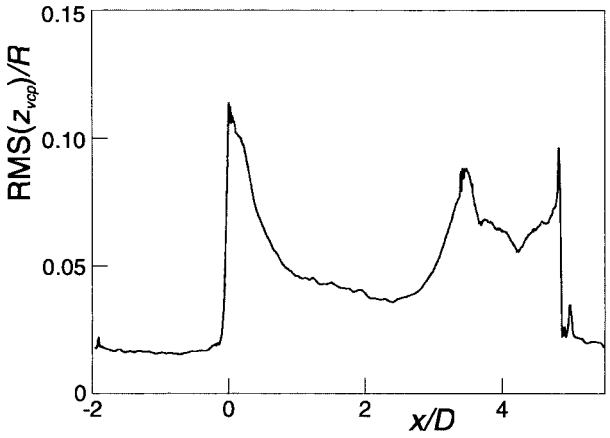

Figure 23. RMS value of the z-coordinate of the vortex center (z_{vcp}) as a function of the axial position in the Stairmand cyclone.

with k_{sgs} the subgrid-scale kinetic energy, $|\mathbf{S}|$ the resolved deformation rate, Δ the grid spacing, and C_{vt} and C_{ε} two constants amounting to 0.05 and 1.0 respectively.

At time equal to $180 \cdot T_{\mathrm{int}}$ after starting the particle injection, about 95% of the injected particles either is in the collection bin, or has been exhausted through the exit pipe. The 5% still inside the body of the cyclone are mainly trapped in a recirculation zone closely beneath the top of the cyclone body, in the annular region between outer wall and exit pipe. The bigger particles very slowly escape from this region due to gravity and subgrid-scale "diffusion". Particle concentration fields are shown in Figure 24. The larger particles are almost immediately trapped in the wall region where they gradually spiral downwards. The smaller the particles, the more they enter the center region where they are convected towards the exit pipe. Figure 25 is a collection efficiency curve (η_{coll} is here defined as the fraction of particles that not escaped through the exit pipe) showing the numerical prediction for the cyclone performance.

5. Summary

Various turbulent flow systems exhibiting swirl as applied in chemical engineering practice have been discussed. Agitated flows (stirred tank) are used for mixing, cyclones for separation. The performance of these devices relies on the turbulent flow field. Process modeling, and performance improvement (in e.g. economic of environmental terms) requires accurate flow field predictions.

In stirred tanks a combined experimental (LDA) and numerical (LES) study on the turbulent wakes behind impeller blades was presented. The experimental, three-dimensional velocity data was used to assess the quality of the LES results. Average velocity fields, and turbulent kinetic energy distributions in the vicinity of the two impellers considered (viz. a Rushton turbine and a pitched blade turbine)

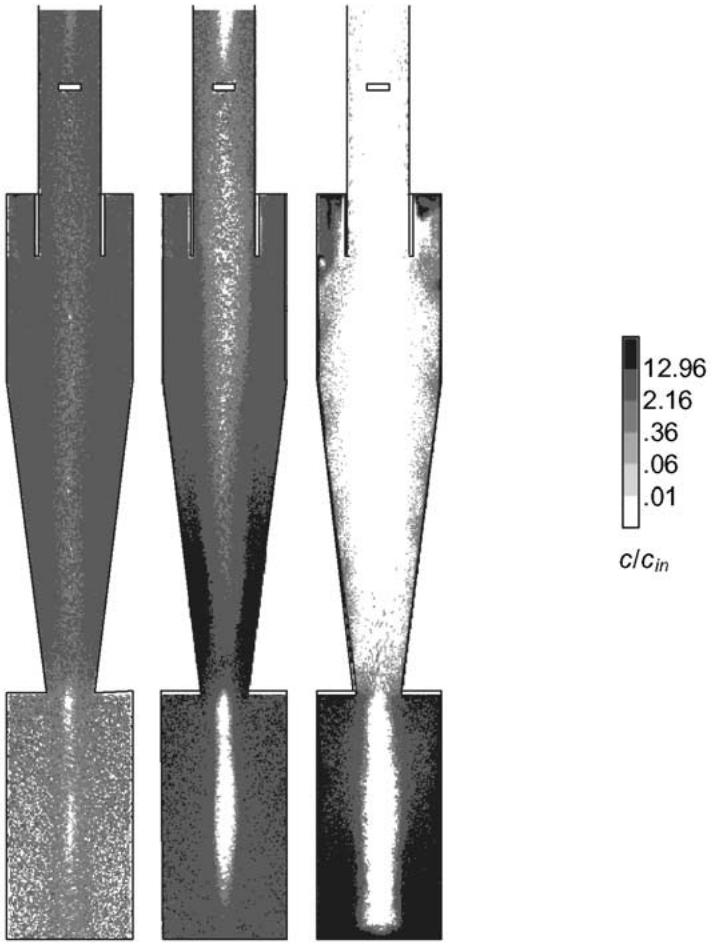

Figure 24. Average particle number concentration in a vertical plane (the plane with $y = 0$) for three values of the Stokes number: from left to right Stk $= 6.5 \cdot 10^{-5}, 1.4 \cdot 10^{-3}, 3.0 \cdot 10^{-2}$.

were predicted fairly accurately. The extent of anisotropy of the Reynolds stress tensor in the wake of a Rushton turbine blade, however, was strongly overestimated. The (obvious) conclusion is that these deviations ask for further research. Primarily, the effect of spatial resolution of the simulations will be investigated. Orthokinetic agglomeration of crystals in a stirred tank was used as an example for the use of detailed (simulated) flow information to study the interplay between hydrodynamics and particle behavior.

The confined swirling flow simulations on a swirl tube and a Stairmand high-efficiency cyclone demonstrated that large-eddy simulations employing the standard Smagorinsky subgrid-scale model extended with Van Driest wall damping functions were well able to capture some of the major flow characteristics of swirling flows: vortex breakdown, spiral-shaped vortex cores, vortex core preces-

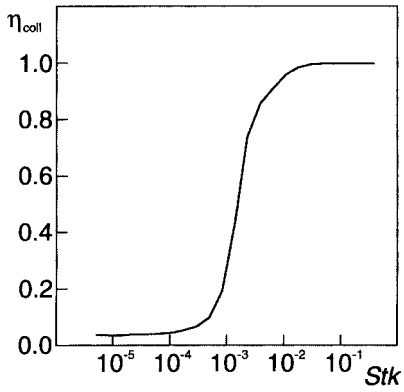

Figure 25. Collection efficiency of the Stairmand high-efficiency cyclone as a function of the Stokes number.

sion. A more quantitative assessment in terms of average velocity profiles, and (for the Stairmand cyclone) velocity fluctuation levels showed grid-resolution effects, and possibly too strong damping of the Smagorinsky model.

In the Stairmand cyclone, vortex core precession was observed. The precession induced high velocity fluctuation levels inside the core of the vortex. The velocity fluctuations appeared to be of a coherent nature. The precession amplitude was a pronounced function of the axial position inside the cyclone. In contrast to the Stairmand cyclone, the vortex core in the swirl tube was very stable (at least in the LES). In practice, vortex core precession is an unwanted phenomenon; it induces vibration that can lead to mechanical failure [14]. Flow simulation might facilitate in proposing design guidelines in order to prevent vortex core precession.

The flow simulations in the Stairmand cyclone were supplemented with solid particle transport (based on one-way coupling) in order to predict the separation performance of the cyclone. The way particles with various sizes were dispersed by the turbulent, swirling flow was visualized.

Acknowledgements

I thank the (former) Ph.D. students Hugo Hartmann, Arjen Hoekstra, and Elco Hollander for their contributions to this article.

References

1. Benjamin, T.B., Theory of the vortex breakdown phenomenon. *J. Fluid Mech.* **14** (1962) 593–629.
2. Burgers, J.M., A mathematical model illustrating the theory of turbulence. *Appl. Mech.* **1** (1948) 171–199.
3. Chen, S. and Doolen, G.D., Lattice Boltzmann method for fluid flows. *Annual Rev. Fluid Mech.* **30** (1998) 329–364.

4. Derksen, J.J. and Van den Akker, H.E.A., Large eddy simulations on the flow driven by a Rushton turbine. *AIChE J.* **45** (1999) 209–221.
5. Derksen, J.J., Doelman, M.S. and Van den Akker, H.E.A., Three-dimensional LDA measurements in the impeller region of a turbulently stirred tank. *Exp. Fluids* **27** (1999) 522–532.
6. Derksen, J.J. and Van den Akker, H.E.A., Simulation of vortex core precession in a reverse-flow cyclone. *AIChE J.* **46** (2000) 1317–1331.
7. Derksen, J., Assessment of large eddy simulations for agitated flows. *Trans IChemE* **79A** (2001) 824–830.
8. Derksen, J.J., Large-eddy simulations on confined swirling flow. In: Rodi, W. and Fueyo, N. (eds.), *Engineering, Turbulence Modeling and Experiments*, Vol. 5. Elsevier, Amsterdam (2002) pp. 907–916.
9. Dyson, J. Vacuum cleaner apparatus. United States Patent No. 5,160,356 (1992).
10. Eggels, J.G.M., Direct and large-eddy simulations of turbulent fluid flow using the lattice-Boltzmann scheme. *Internat. J. Heat Fluid Flow* **17** (1996) 307–323.
11. Escudier, M.P., Bornstein, J. and Zehnder, N., Observations and LDA measurements of confined turbulent vortex flow. *J. Fluid Mech.* **98** (1980). 49–63.
12. Escudier, M.P., Bornstein, J. and Maxworthy, T., The dynamics of confined vortices. *Proc. Roy. Soc. London A* **382** (1982) 335–360.
13. Faler, J.H. and Leibovich, S., Disrupted states of vortex flow and vortex breakdown. *Phys. Fluids* **20** (1977) 1385–1400.
14. Gupta, A.K., Lilley, D.G. and Syred, N., *Swirl Flows*. Abacus Press, Tunbridge Wells (1984) 475 pp.
15. Hinze, J.O., *Turbulence*. McGraw-Hill, New York (1959). 586 pp.
16. Hoekstra, A.J., Derksen, J.J. and Van den Akker, H.E.A., An experimental and numerical study of turbulent swirling flow in gas cyclones. *Chem. Engrg. Sci*. **54** (1999) 2055–2065.
17. Hoekstra, A.J., Gas flow and collection efficiency of cyclone separators. Ph.D. Thesis, Delft University of Technology (2000) 165 pp.
18. Hollander, E.D., Derksen, J.J., Portela, L.M. and Van den Akker, H.E.A., Numerical scale-up study for orthokinetic agglomeration in stirred vessels. *AIChE J.* **47** (2001) 2425–2440.
19. Lee, K.C. and Yianneskis, M., Turbulence properties of the impeller stream of a Rushton turbine. *AIChE J*. **44** (1998) 13–25.
20. Lopez, J.M., Marques, F. and Sanchez, J., Oscillatory modes in an enclosed swirling flow. *J. Fluid Mech.* **439** (2001) 109–129.
21. Lumley, J., Computational modeling of turbulent flows, *Adv. Appl. Mech*. **26** (1978) 123–176.
22. Mumtaz, H.S., Hounslow, M.J., Seaton, N.A., Paterson, W.R., Orthokinetic aggregation during precipitation, a computational model for Calcium Oxalate Monohydrate. *Trans. IChem. E*. **75** (1997) 152–159.
23. Rushton, J.H., Costich, E.W. and Everett, H.J., Power characteristics of mixing impeller I and II. *Chem. Engrg. Progr*. **46** (1950) 395–404 and 467–476.
24. Schäfer, M., Yianneskis, M., Wächter, P. and F. Durst, Trailing vortices around a 45° pitched-blade impeller. *AIChE J.* **44** (1998) 1233–1246.
25. Serre, E. and Bontoux, P., Three-dimensional swirling flow with a precessing vortex breakdown in a rotor-stator cylinder. *Phys. Fluids* **13** (2001) 3500–3503.
26. Sharp, K.V. and Adrian, R.J., PIV study of small-scale flow structure around a Rushton turbine. *AIChE J*. **47** (2001) 766–778.
27. Smagorinsky J., General circulation experiments with the primitive equations: Part I, The basic experiment. *Monthly Weather Rev.* **91** (1963) 99–164.
28. Snyder, D.E. and Spall, R.E., Numerical simulation of bubble-type vortex breakdown within a tube-and-vane apparatus. *Phys. Fluids* **12** (2000) 603–608.
29. Somers, J.A., Direct simulation of fluid flow with cellular automata and the lattice-Boltzmann equation. *Appl. Sci. Res.* **51** (1993) 127–133.

30. Sotiropoulos, F. and Ventikos, Y., Transition from bubble-type vortex breakdown to columnar vortex in a confined swirling flow. *Internat. J. Heat Fluid Flow* **19** (1998) 446–458.
31. Sotiropoulos, F. and Ventikos, Y., The three-dimensional structure of confined swirling flows with vortex breakdown. *J. Fluid Mech*. **426** (2001) 155–175.
32. Spall, R.E. and Ashby, B.M., A numerical study of vortex breakdown in turbulent swirling flows. *J. Fluids Engrg*. **122** (2000) 179–183.
33. Stairmand, C.J., The design and performance of cyclone separators. *Trans. IChem. E*. **29** (1951) 356–383.
34. Stoots, C.M. and Calabrese, R.V., Mean velocity field relative to a Rushton turbine blade. *AIChE J*. **41** (1995) 1.
35. Taniguchi, N., Lei, K., Takenaka, K. and Kobayashi, T., Evaluation of subgrid scale models for the large eddy simulation of particle laden flow. In: *Proceedings of the 3rd ASME/JSME Joint Fluids Engineering Conference*, Vol. FEDSM99-7370. ASME, New York (1999) pp. 1–6.
36. Van 't Riet, K. and Smith, J.M., The trailing vortex system produced by Rushton turbine agitators. *Chem. Engrg. Sci*. **30** (1975) 1093–1105.
37. Voke, P.R., Subgrid-scale modelling at low mesh Reynolds number. *Theor. Comput. Fluid Dynam.* **8** (1996) 131–143.
38. Wu, H. and Patterson, G.K., Laser-Doppler measurements of turbulent-flow parameters in a stirred mixer. *Chem. Engrg. Sci*. **44** (1987) 2207–2221.
39. Yianneskis, M., Popiolek, Z. and Whitelaw, J.H., An experimental study of the steady and unsteady flow characteristics of stirred reactors. *J. Fluid Mech*. **175** (1987) 537–555.